CHEMISTRY OF MATERIALS

Article

pubs.acs.org/cm

Electrochemical Stability of Metastable Materials

Arunima K. Singh,[*,†] Lan Zhou,[‡] Aniketa Shinde,[‡] Santosh K. Suram,[‡] Joseph H. Montoya,[§] Donald Winston,[§] John M. Gregoire,[‡] and Kristin A. Persson[*,∥,⊥]

[†]Joint Center for Artificial Photosynthesis and [∥]Environmental Energy Technologies Division, Lawrence Berkeley National Laboratory, Berkeley, California 94720, United States

[‡]Joint Center for Artificial Photosynthesis, California Institute of Technology, Pasadena, California 91125, United States

[§]Lawrence Berkeley National Laboratory, Berkeley, California 94720, United States

[⊥]Department of Materials Science and Engineering, University of California, Berkeley, California 94720, United States

Supporting Information

ABSTRACT: We present a first-principles-based formalism to provide a quantitative measure of the thermodynamic instability and propensity for electrochemical stabilization, passivation, or corrosion of metastable materials in aqueous media. We demonstrate that this formalism can assess the relative Gibbs free energy of candidate materials in aqueous media as well as their decomposition products, combining solid and aqueous phases, as a function of pH and potential. On the basis of benchmarking against 20 stable as well as metastable materials reported in the literature and also our experimental characterization of metastable triclinic-$FeVO_4$, we present quantitative estimates for the relative Gibbs free energy and corresponding aqueous regimes where these materials are most likely to be stable, form inert passivating films, or steadily corrode to aqueous species. Furthermore, we show that the structure and composition of the passivating films formed on triclinic-$FeVO_4$ are also in excellent agreement with the Point Defect Model, as proposed by the corrosion community. An open-source web application based on the formalism is made available at https://materialsproject.org.

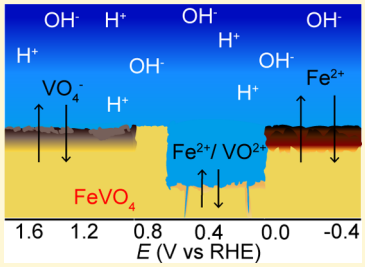

INTRODUCTION

The economic cost of environmental degradation of materials has been estimated to be over 200 billion dollars in the U.S. economy alone.[1] Corrosion management, improvement in performance, and an increased operational life of materials for household appliances, infrastructure, vehicles, and manufacturing calls for an improved understanding of materials stability under varying alkalinity, humidity, temperature, and pollutant conditions. Furthermore, aqueous media-based electrochemical processes such as water purification and catalysis routinely operate devices at finite potentials and pH where materials stability is strikingly different from ambient conditions.

A concise equilibrium thermodynamics-based understanding of elemental corrosion in aqueous media can be accurately obtained from the so-called Pourbaix diagrams which indicate the potential and pH ranges where the different multicomponent oxidation states of materials exist. Marcel Pourbaix and others have collected thermodynamic data for reactions involving metals, their ions, their oxides, and occasionally sulfides, providing the electrochemical phase diagrams for ca. 85 elements in the periodic table.[2−4] While the electrochemical stability of elements has been studied extensively, only a small fraction of binary materials and seldom ternary and higher-component materials have been investigated experimentally.

Recently, Persson et al. used first-principles density-functional theory (DFT)-based thermodynamic energies of solids in conjunction with experimentally available ion and aqueous species energies to predict Pourbaix diagrams of n-component materials (n = 1 to ∞).[5] This formalism has reproduced the thermodynamic electrochemical stability of all experimentally investigated n = 1 systems, and to date, successfully predicted the electrochemical stability of several complex materials such as $Mn_2V_2O_7$,[6] $MnNiO_3$, Cu−V−oxides,[7] and nanoclusters.[8] In principle, Pourbaix diagrams account for materials only at thermodynamic equilibrium, providing no insight into the electrochemical stability of metastable materials which find practical applications in many commercial applications and research such as steels,[9] ceramics,[10] photocatalysis,[11] and optoelectronics.[12] Furthermore, among the 29 902 unique bulk crystalline phases reported in the Inorganic Crystal Structure Database (ICSD),[13] the first-principles-based, zero-temperature Materials Project database computations predict that 50.5 ± 4% (15 097) of the experimentally synthesized structures are metastable solid-state phases.[14]

We expand the formalism of Persson et al. to enable the evaluation of the relative Gibbs free energy of metastable materials as a function of pH, potential, temperature, and concentration of aqueous species. Note that while this formalism accounts for the experimentally measured entropy of several gases, water and all aqueous species, we neglect the entropic contributions for the solids toward Gibbs free energies since the solid−solid entropy differences are likely to be orders

Received: September 19, 2017
Revised: October 18, 2017
Published: October 24, 2017

DOI: 10.1021/acs.chemmater.7b03980
Chem. Mater. 2017, 29, 10159−10167

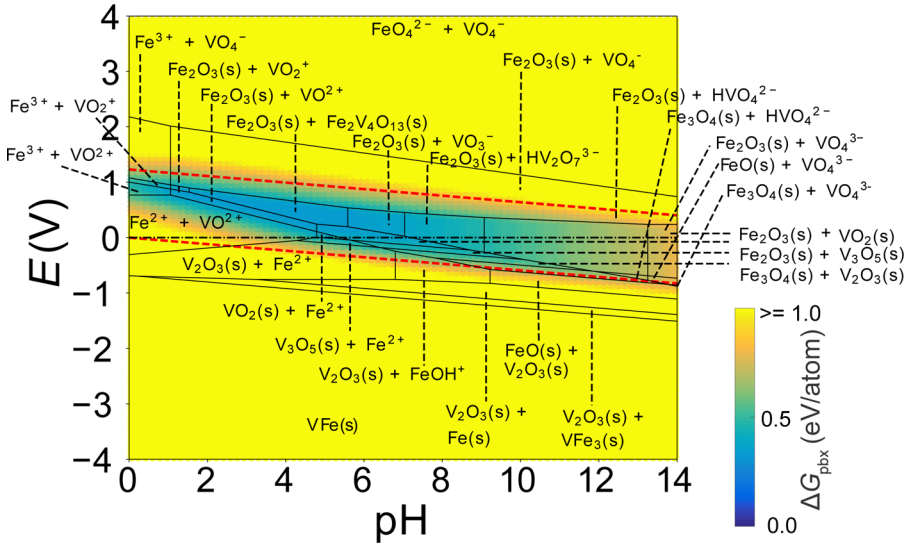

Figure 1. Computationally predicted Pourbaix diagram of the Fe−V−O−H system. The Gibbs free energy, ΔG_{pbx}, of the metastable triclinic-$FeVO_4$ phase with respect to the Pourbaix stable phases is superimposed and represented by the color bar. The lowest value of ΔG_{pbx} for $FeVO_4$ is 0.34 eV/atom at pH 1.63 and voltage of E = 0.85 V, where it is predicted to phase transform to $Fe_2V_4O_{13}$ and Fe_2O_3, a solid-state reaction enabled by the stability of both reaction products under this electrochemical condition. The red dashed lines denote potentials of 0 V vs RHE and 1.23 V vs RHE.

of magnitude smaller than the enthalpic contributions at room temperature.[15] We demonstrate that materials with decomposition Gibbs free energies as high as 0.5 eV/atom have been reported as stable against corrosion due to self-passivation and formation of more stable solid-state surface phases. An excellent correlation is found between the Gibbs free energy and propensity of 20 materials (including GaP, $Zn(FeO_2)_2$, Si, WSe_2, GaAs, Fe_2O_3, WO_3, and TiO_2) reported in the experimental literature, to be stable, passivate or corrode. In addition, we grow the metastable triclinic-$FeVO_4$ phase and show that the electrochemical response of $FeVO_4$ is in excellent agreement with the computational predictions with respect to both the stability and composition of the self-passivated layers, as applicable. The instability landscape reported in this article provides a critical guide toward environmental degradation management as well as design of metastable materials or protective films in materials of all classes for aqueous media-based applications. Further, we suggest that an a priori knowledge of the passivation layer composition can aid the kinetic and phenomenological Point Defect Model[16] to predict the microstructure, passivation layer thickness, and the kinetic stability of self-passivating films.

The formalism is made available through a user-friendly web-based app which allows for the generation and assessment of the metastability of over 69 000 materials, including estimation of pH, concentration, and potential dependent composition of possible passivation layers, available at https://materialsproject.org.

METHODS

Mapping Pourbaix diagrams for multicomponent systems requires the knowledge of equilibrium redox reactions as well as the standard state reaction Gibbs free energy of each redox reaction, $\Delta_r G°$. For example, a binary M−X system in aqueous media can result in a redox reaction such as

$$aM(s) + bX(s) + cH_2O(l) \rightarrow M_aX_bO_cH_d^m(aq) + (2c - d)H^+ + (2c - d + m)e^- \quad (1)$$

where a, b, c, and d are the stoichiometric coefficients of M, X, O, and H, respectively, and m is the charge on the aqueous species $M_aX_bO_cH_d^m$ which could be positive, negative, or zero. The number of competing redox reactions scales rapidly with the number of elements considered to compute the Pourbaix diagram. For instance, for a Fe−V system, there are 11 experimentally reported Fe-containing and 14 V-containing (positively charged, negatively charged, or neutral) aqueous species, along with 14 ground-state solids containing one or more of Fe, V, or O elements. At equilibrium, the Nernst equation can be used to relate the cell potential, $E°$, to the reaction Gibbs free energy, $\Delta_r G$, for each possible redox reaction. For instance,

$$-\nu\ F\ E^o = \Delta_r G = \Delta_r G^o + R\ T\ \ln Q \quad (2)$$

$$= \Delta_r G^o + R\ T\ \ln\left[\frac{(a_P)^p.(a_{H^+})^h}{(a_R)^r.(a_{H_2O})^w}\right] \quad (3)$$

$$= \Delta_r G^o + 2.303\ R\ T\ \log\left[\frac{(a_P)^p}{(a_R)^r.(a_{H_2O})^w}\right] - 2.303\ h\ R\ T\ \mathrm{pH} \quad (4)$$

where T is the temperature, F is the Faraday constant, R is the ideal gas constant, pH is $-\log(H^+)$, $\nu = (2c - d + m)$ is the number of electrons, $a_R^r = a_{M(s)}^a a_{X(s)}^b$ is the activity of the reactants, $a_P^p = a_{M_aX_bO_cH_d^m}^m$ is the activity of the products, $a_{H_2O}^w = a_{H_2O}^c$ is the activity of water, and $a_{H^+}^h = a_{H^+}^{(2c-d)}$ is the activity of hydrogen ions for the reaction in eq 1. In principle, identifying the redox reaction that minimizes the difference between the contribution from the cell potential and the reaction Gibbs free energy, $\min(\Delta_r G + \nu FE^0)$, is sufficient to identify the range of pH and E where a particular solid or ionic species is stabilized over others for a given temperature, concentration of ions, and stiochiometry of elements under consideration.

However, the lack of complete knowledge of possible redox reactions is the limiting factor in this analysis. In previous efforts, computed crystalline solid energies have been combined with experimentally measured free energies of aqueous species, which are readily available in thermodynamic databases.[5] A thorough description of the scheme of reference energies which allows for the combination of experimental and computational thermodynamic data can be found in ref 5. Furthermore, computational materials data are available in larger and more comprehensive quantities than ever before through efforts like The Materials Project,[17] OQMD,[18] and aflowlib.[19] The experimentally measured energies of aqueous species,[2,3,15,20,21] totaling 362, corresponding to 80 elements in the periodic table, are also available through the Materials Project API.[22] Among the 69 640

DOI: 10.1021/acs.chemmater.7b03980
Chem. Mater. 2017, 29, 10159−10167

currently available materials in the Materials Project database, 34 913 materials correspond to compounds in the ICSD, 23 776 are ground states, and the intersection of these sets contains 18 993 compounds. In conjunction with 362 ionic energies for 80 elements in the periodic table, the electrochemical stability for the 23 776 ground-state structures can already be determined.

We update the formalism of Persson et al.[5] to include redox reactions corresponding to an arbitrary metastable material. Metastable materials cannot result in thermodynamically favorable redox reactions; thus, we estimate their Gibbs free energy difference with respect to the Pourbaix stable domains as a function of pH and E, providing electrochemical instability maps for arbitrary metastable materials. This Gibbs free energy difference, ΔG_{pbx}, thus includes the instabilities arising from the enthalpy difference with respect to the likely decomposition products of the metastable material at zero pressure and zero temperature, also known as energy above the convex hull, ΔH_{solid}, and contributions from the pH and voltage factors of eq 4. For detailed information on the mathematical implementation, please refer to the pymatgen python package.[23]

As an example, Figure 1 shows the Pourbaix diagram of the Fe−V−O−H system with a 1:1 composition of Fe and V in an infinite reservoir of water. An ionic concentration of 10^{-5} M of both Fe and V species, an activity of solids of 1, temperature of 298 K, and a pressure of 1 atm is used for the analysis of Fe−V−O−H and all systems described henceforth, unless otherwise noted. The ground-state solids relevant to the Fe−V−O−H system, that is, FeO, Fe_2O_3, Fe_3O_4, $Fe_2V_4O_{13}$, Fe_3V, FeV, VO_2, V_2O_3, V_3O_4, and V_2O_5, are mapped in the Pourbaix diagram, and their stability regions can be identified through inspection of the figure. However, the metastable triclinic phase of $FeVO_4$ is not visibly represented in the equilibrium Pourbaix diagram. Under ambient pressure, this phase exhibits a ΔH_{solid} = 0.34 eV/atom for a 1:1 spontaneous decomposition to the stable Fe_2O_3 and $Fe_2V_4O_{13}$ solids. The ΔG_{pbx} with respect to the Pourbaix stable domains, superimposed on the Pourbaix diagram, enables estimation of the instability of $FeVO_4$ against all possible combinations of solid as well as aqueous species. We note that the most favorable ΔG_{pbx} for $FeVO_4$ occurs where it is expected to decompose into $Fe_2V_4O_{13}$ and Fe_2O_3 in equal amounts to maintain the 1:1 stoichiometry of Fe and V. The minimum of the ΔG_{pbx} = 0.34 eV/atom is found at pH 1.63 and E = 1.85 V, which includes the ΔH_{solid} and no contributions from the potential and pH factors are expected based on the redox reactions. The ΔG_{pbx} increases rapidly beyond the stability domain of $Fe_2V_4O_{13}$ and Fe_2O_3, indicating that it is progressively likely that the Pourbaix-determined phases will be more favorable than the metastable $FeVO_4$. Similar plots were created for all the materials studied in this work.

To assess the ΔG_{pbx}, which can be tolerated due to high barriers for solid−solid phase transformations or mitigated by dissolution−precipitation-assisted surface passivation, we compare the predicted ΔG_{pbx} with the electrochemical behavior of materials reported in the experimental literature. In the next section we show examples of materials with ΔG_{pbx} up to 0.5 eV/atom have been experimentally reported as stable within some observation time. While the thermodynamic driving force for dissolution is an important metric, we find that it is equally important to consider the nature of the decomposition products, for example, whether they form aqueous ions, solid phases, or a combination thereof. For materials where $\Delta G_{pbx} > 0$ and self-passivating layers form on the surface of the materials, we show that the predicted passivation layer compositions are in agreement with experimentally observed passivation layer compositions.

Methods for the model validation experiments are described in the Supporting Information.

RESULTS AND DISCUSSION

Validation Against Experimental Reports in the Literature. Figure 2 shows the theoretically computed ΔG_{pbx} for ca. 20 well-known photoanode materials. We choose photoanode materials for a comparison of the theoretical predictions with experimental reports in the literature since

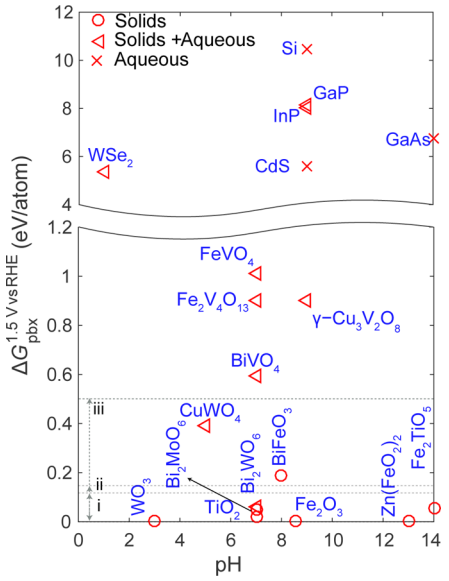

Figure 2. ΔG_{pbx} of photoanode materials at 1.5 V vs RHE at pH values corresponding to those in experimental reports, listed in Table 1. Materials which are expected to remain stable or decompose to only solid species are shown as circles. Those which decompose to solids as well as aqueous species are shown as triangles and the ones which are expected to dissociate to only aqueous species are shown as cross symbols. Refer to Table 1 for details of the decomposed species. The driving forces to stabilize materials with energies marked in region (i) can be due to ionic concentration fluctuations, those marked in region (ii) could be due to temperature fluctuations and those by region (iii) due to activation energy barriers. Furthermore, operational stability can also be obtained due to formation of inert passivation layers.

numerous studies report the electrochemical stability of photoanode materials. After the discovery of the first photoanode material in 1972, TiO_2,[24] over 130 semiconductors, including oxides, sulfides, and phosphides,[11] have been extensively studied to improve, among other properties, their aqueous stability and operational life. The ΔG_{pbx} is computed for a potential of 1.5 V vs RHE (which accounts for the 1.23 eV free energy of water splitting and an overpotential of 0.27 eV that is typically required for electrocatalysis) and pH values corresponding to the experimental measurements in the literature (Table 1).

The 12 metastable materials, anatase−TiO_2, α-$Cu_2V_2O_7$, α-CuV_2O_6, $BiVO_4$, γ-$Cu_3V_2O_8$, $BiFeO_3$, Fe_2TiO_5, α-$Cu_3V_2O_8$, $Cu_{11}V_6O_{26}$, $CuWO_4$, FeV_2O_4, and $FeVO_4$ have ΔH_{solid} ranging from 0.01 eV/atom, for anatase−TiO_2, to 0.11 eV/atom, for $FeVO_4$. The remaining 13 materials, $Zn(FeO_2)_2$, Bi_2MoO_6, WO_3, Fe_2O_3, Bi_2WO_6, $Fe_2V_4O_{13}$, β-$Cu_2V_2O_7$, WSe_2, CdS, GaAs, InP, GaP, and Si, are thermodynamically stable materials, that is, their ΔH_{solid} = 0 eV/atom.

Evidently, the ΔG_{pbx} should be zero for the electrochemically stable compounds. However, somewhat surprisingly, excluding the spinel $ZnFe_2O_4$ and the orthorhombic WO_3, all the materials which are found to be stable experimentally have a $\Delta G_{pbx} > 0$, up to 0.5 eV/atom. Our calculations predict that WO_3 has a ΔG_{pbx} = 0 for pH < 4 solutions and it has also been reported to be stable experimentally at pH < 4.[25,26] Furthermore, at higher pH values it has been observed to corrode, which is in agreement with the prediction that the orthorhombic WO_3 should dissolve as WO_4^- ions with ΔG_{pbx} of up to 1 eV/atom. The spinel structure of $ZnFe_2O_4$ has ΔG_{pbx} = 0 eV/atom over a large alkaline range, pH 7−14; however, no

DOI: 10.1021/acs.chemmater.7b03980
Chem. Mater. 2017, 29, 10159−10167

Table 1. Predicted Stable Species in Aqueous Media, Decomposed Species, and ΔG_{pbx}, in eV/atom, of 25 Materials in Water at 1.5 V vs RHE[a]

material	ΔG_{pbx}	pH_{Exp}	decomposed species	mp-id	reference
$Zn(FeO_2)_2$	0.00	13	$Zn(FeO_2)_2$ (s)	mp-19313	27, 28
WO_3	0.00	3	WO_3 (s)	mp-19342	25
Fe_2O_3	0.00	9	Fe_2O_3 (s)	mp-24972	29, 31
TiO_2	0.02	7	TiO_2 (s)	mp-390	30, 31
Bi_2MoO_6	0.05	7	Bi_2MoO_6 (s)	mp-25708	32
Fe_2TiO_5	0.06	14	Fe_2O_3 (s) + TiO_2 (s)	mp-24977	39
Bi_2WO_6	0.06	7	Bi_4O_7 (s) + WO_4^{2-}	mp-25730	33
$BiFeO_3$	0.19	8	Fe_2O_3 (s) + Bi_4O_7 (s)	mp-24932	34, 35
$CuWO_4$	0.39	5	Cu_2O_3 (s) + WO_4^{2-}	mp-510632	26, 40
$BiVO_4$	0.59	7	Bi_4O_7 (s) + VO_4^-	mp-504878	36−38
$Cu_{11}V_6O_{26}$	0.87	9	Cu_2O_3 (s) + VO_4^-	mp-505456	7, 41
$Fe_2V_4O_{13}$	0.90	7	Fe_2O_3 (s) + VO_4^-	mp-565529	42
γ-$Cu_3V_2O_8$	0.90	9	Cu_2O_3 (s) + VO_4^-	mp-504747	7, 41, 43
α-$Cu_3V_2O_8$	0.92	9	Cu_2O_3 (s) + VO_4^-	mp-600273	7, 41
β-$Cu_2V_2O_7$	1.00	9	Cu_2O_3 (s) + VO_4^-	mp-559660	7, 44
$FeVO_4$	1.01	7	Fe_2O_3 (s) + VO_4^-	mp-540630	45, 46
α-$Cu_2V_2O_7$	1.02	9	Cu_2O_3 (s) + VO_4^-	mp-505508	7, 44
α-CuV_2O_6	1.28	9	Cu_2O_3 (s) + VO_4^-	mp-741706	7, 47
FeV_2O_4	3.10	7	Fe_2O_3 (s) + VO_4^-	mp-510496	45
WSe_2	5.38	1	WO_3 (s) + $HSeO_4^-$	mp-1821	48
CdS	5.58	9	Cd^{2+} + SO_4^{2-}	mp-672	49, 50
GaAs	6.77	14	AsO_4^{3-} + GaO_3^{3-}	mp-2534	25, 31, 51, 52
InP	8.01	9	In_2O_3 (s) + HPO_4^{2-}	mp-20351	25, 53
GaP	8.15	9	Ga_2O_3 (s) + HPO_4^{2-}	mp-2490	25, 31
Si	10.45	9	H_4SiO_4 (aq)	mp-149	25, 31

[a]The pH values, pH_{Exp}, correspond to the pH values in the measurements carried out in the listed references. The Materials Project material ids (mp-id) corresponding to the materials are listed as well.

experimental reports of the electrochemical stability could be identified in the literature.[27,28] For further details, see Figure S1 in the Supporting Information for pH-dependent ΔG_{pbx} and decomposition products of all the materials at 1.5 V (all voltages here on are vs RHE).

Among those materials which exhibit a $\Delta G_{pbx} > 0$ but are still found to be stable experimentally, Fe_2O_3 exhibits a ΔG_{pbx} = 0.001 eV/atom at pH 2−12 which is within the numerical accuracy of DFT. Experimental measurements are in excellent agreement, showing that Fe_2O_3 indeed exhibits a large pH stability window from 2 to 14.[29] The widely used photoanode, anatase−TiO_2, also has a small ΔG_{pbx} = 0.02 eV/atom against the formation of its polymorph α-TiO_2. This small ΔG_{pbx} is found to be insufficient to drive a solid−solid phase transformation and hence anatase−TiO_2 is found to be extremely robust in both alkaline and acidic regions, pH 0−14.[30,31] Bi_2MoO_6 has a slightly larger ΔG_{pbx} = 0.05 eV/atom and is predicted to dissociate to Bi_4O_7 and MoO_4^- at pH 7 and 1.4 V, but is found to be stable experimentally.[32] At pH 7, Bi_2WO_6 has a ΔG_{pbx} = 0.06 eV/atom, comparable to that of Bi_2MoO_6. Our formalism predicts a thermodynamic liability to dissociate to Bi_2O_4 and WO_4^{2-} under these conditions. Yet, experimentally it has been observed to exhibit no significant drop in photocurrent and no obvious change in the morphology.[33] Another material which remains stable despite a $\Delta G_{pbx} > 0$ is $FeBiO_3$, which at pH 7.5 and 1.7 V is found to be operationally stable despite the predicted dissociation into Fe_2O_3 and $Bi_4O_7^-$ [34,35] as expected from our thermodynamic predictions. The most extreme of these examples is the monoclinic scheelite $BiVO_4$ which has attracted recent interest due to conflicting reports of aqueous stability. The material was deemed stable[36] at pH 7 which corresponds to a very large ΔG_{pbx} = 0.59. Similarly, at pH 6.6, E = 1.41 V, where ΔG_{pbx} = 0.45 eV/atom, no change in the X-ray diffraction (XRD) pattern or optical absorbance of $BiVO_4$ was observed.[37] On the other hand, recent combined experimental and computational work shows that $BiVO_4$ corrodes in alkaline pH at 1.23 V.[38]

In contrast, materials with $\Delta G_{pbx} > 5.5$ eV/atom, that is, Si, GaAs, InP, CdS, and InP, corrode vigorously.[49−52] We note that these five materials are predicted to either decompose to only aqueous or a combination of oxides and aqueous species. None of them exhibit instability to only solid phases. Consequently, these materials are coated with more stable materials such as TiO_2 and Fe_2O_3[31,53] when used as photoanodes.

All other examined materials are found to self-passivate with passivation layers whose compositions are in excellent agreement with those predicted theoretically. For instance, WSe_2 is predicted to dissociate to WO_3 and solvated Se atoms as $HSeO_4^-$ ions with a ΔG_{pbx} = 4.96 eV/atom at pH 1 and E = 1.43 V, in excellent agreement with the experimental observation that, in perchloric acid, pH 0.4−1.0, and at 1.43 V, WSe_2 forms a thin porous WO_3 passivation layer.[48] In another case, it is observed experimentally that mesoporous films of Fe_2TiO_5 form self-passivating films composed of a mixture of mesoporous Fe_2TiO_5, Fe_2O_3, and Fe-doped anatase−TiO_2[39] at pH 13.9. Even though a direct comparison cannot be made between the experiments for the mesoporous Fe_2TiO_5 and our calculations for crystalline Fe_2TiO_5, we predict that crystalline Fe_2TiO_5 should indeed decompose to Fe_2O_3 and TiO_2 with a ΔG_{pbx} = 0.06 eV/atom. Another class of materials, copper vanadates, are shown to form self-passivating layers in the alkaline region[7,41,44] at pH 7−13. This is in agreement with the large ΔG_{pbx} of the Cu vanadates, exceeding 1 eV/atom, and a prediction that they dissociate to Cu_2O_3 and VO_4^- ions in aqueous solution.

Several other experimental reports provide indirect evidence for the formation of self-passivation layers. For example, FeV_2O_4 at pH 7 is found to remain almost stable with about 20% change in current density at 1.0 V.[45] It is likely that the reduction in the current density could be due to the formation of Fe_2O_3 passivation layers when V dissolves as VO_4^-. However, photodegradation and formation of solid electrolyte deposits could also be a cause of the decrease in FeV_2O_4 film's current density. Similar Gibbs free energy based metric was

DOI: 10.1021/acs.chemmater.7b03980
Chem. Mater. 2017, 29, 10159−10167

used to predict the aqueous stability of Li- and Na-based materials which are used as solid electrolytes.[54] However, stability and passivation film composition were not verified due to limited experimental literature.

Hence, we surmise that materials with ΔG_{pbx} up to high values of as much as 0.5 eV/atom can persist in electrochemical environments due to two possible reasons. First, the energy gained via dissociation to the Pourbaix stable domains may not be sufficient to overcome the energy barrier for the dissociation reactions. Energy barriers for bulk solid-state transformations are found to be well below 1 eV/atom, greatly depending on the system under consideration.[55−58] Second, if the decomposition products include a major contribution from solid-state phase(s), preferential dissolution of some species can enable formation of a self-passivating interphase, which will protect the underlying material. Furthermore, we note that fluctuations in the ionic concentration and temperature can contribute significantly to the corrosion/passivation process. For example, 2 orders of magnitude increase in the ionic concentration can result in up to $2 \times 2.303 \times RT/F$ (0.118 eV/atom for T = 298 K or 0.128 eV/atom for T = 323 K) reduction in the decomposition energy. Considering possible selective thermodynamic dissolution and precipitation of different species, it is likely that materials will be immune to corrosion by self-passivation at ΔG_{pbx} energies which are of the order of a fraction of an eV/atom. Needless to say, the maximum ΔG_{pbx} up to which a material is stable is very much dependent on the system and small changes in the ionic concentration or small adjustments in pH and potential can be helpful in stabilizing materials.

While crystalline materials were used as inputs for the theoretical analysis, the experimental reports of the 20 materials encompassed crystalline, amorphous, and porous phases synthesized under different conditions. These materials comprise different chemistries—oxides, phosphides, sulfides, selenides, and arsenides—and were investigated under different electrolytes and electrolyte concentrations. In addition, while the photoanode surfaces were characterized carefully in some reports, the stability and surface composition of several photoanodes were more indirect.

Experimental Validation for Triclinic-$FeVO_4$. As further validation of our methodology and to explore the importance of our identification and classification of decomposition products, we perform experiments based on the calculations of Figure 1. A thin film of the metastable triclinic-$FeVO_4$, which has ΔH_{solid} = 0.11 eV/atom, was grown via sputtering (see Supporting Information). We studied the elemental etch rates and surface compositions before and after the electrochemical reactions at various voltages in an acidic solution of pH 2.9 and compared them to our calculations.

Table 2 shows the electrochemical response of $FeVO_4$ at this pH for various voltages as expected from our calculations. At voltages of −0.4 and 0.0 V, $FeVO_4$ is expected to form a coating of bixbyite-type V_2O_3 concurrently losing Fe as Fe^{2+} ions. At the voltage of 0.4 V our calculations predict it to corrode into primarily Fe^{2+} and VO^{2+} ions. At a higher voltage of 0.8 V it is predicted to phase transform into monoclinic $Fe_2V_4O_{13}$ and α-Fe_2O_3. Finally, at 1.2 and 1.6 V a coating of α-Fe_2O_3 is expected with loss of V as VO_4^- ions.

A thin film composition library of $Fe_{1-x}V_xO_z$ was synthesized by combinatorial sputtering of Fe and V metal targets on fluorine-doped tin oxide (FTO)-coated glass substrate. The $FeVO_4$ phase-pure regions in this composition library were determined using XRD. As expected, X-ray photoelectron spectroscopy (XPS, performed after air exposure) revealed the presence of Fe^{3+} and V^{5+} in these samples in approximately equal amounts (see Figure S3). To assess the electrochemical stability of these phase-pure $FeVO_4$ samples, six as-deposited samples were polarized at −0.4, 0.0, 0.4, 0.8, 1.2, and 1.6 V (separately) in an aqueous electrolyte solution buffered at pH 2.9 (0.1 M potassium phosphate, 0.04 M phosphoric acid with 0.25 M sodium sulfate) for 15 min. To maintain a low ionic concentration in the solution over the course of this electrochemical process, it was performed in a scanning droplet cell with a rapid solution flow (approximately 0.5 L cm^{-2} s^{-1}) over the working electrode. XRD-determined phases, the X-ray fluorescence (XRF)-determined molar concentrations of Fe and V and the XPS-determined surface compositions, were measured both before and after exposure to the aqueous electrochemical environment.

As the entire film thickness is within the sampling depth of XRF, comparison of the pre- and postelectrochemistry Fe and V molar concentrations provides an estimate of the average elemental etching rate during the experiments. Two example XRF spectra of films pre- and postelectrochemistry at potentials of 0.4 and 0.8 V are shown in parts (a) and (b), respectively, of Figure 3. The V K_α and Fe K_α peaks were used for quantification of elemental concentrations and ultimately the

Table 2. Predicted Stable Species in Aqueous Media, Decomposed Species, and ΔG_{pbx} of the Triclinic-$FeVO_4$ in Water at a pH of 2.9 and Potentials, E, Ranging from −0.4 to 1.6 V vs RHE

E vs RHE	ΔG_{pbx} (eV/atom)	decomposed species
−0.4	1.64	V_2O_3 (s) + Fe^{2+}
0.0	1.04	V_2O_3 (s) + Fe^{2+}
0.4	0.62	Fe^{2+} + VO^{2+}
0.8	0.34	$Fe_2V_4O_{13}$ (s) + Fe_2O_3 (s)
1.2	0.59	Fe_2O_3 (s) + VO_4^-
1.6	0.99	Fe_2O_3 (s) + VO_4^-

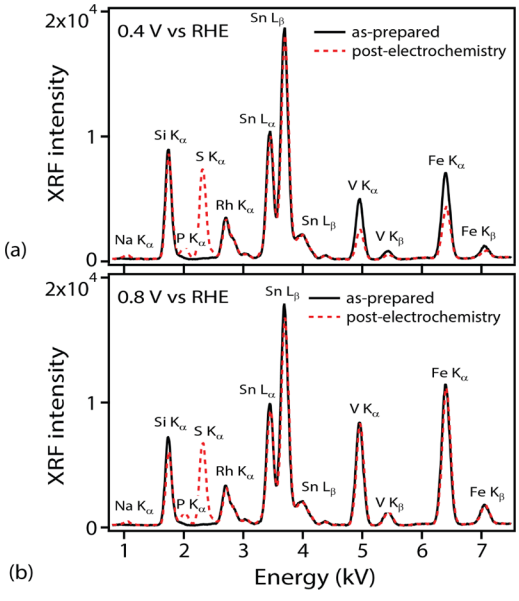

Figure 3. XRF spectra for $FeVO_4$ sample before and after 15 min electrochemical stability measurement in pH 2.9 under the potential of (a) 0.4 V and (b) 0.8 V vs RHE.

DOI: 10.1021/acs.chemmater.7b03980
Chem. Mater. 2017, 29, 10159−10167

average etch rates shown in Figure 4a. At 0.4 V, about 50% drop in the intensities of these peaks indicates that

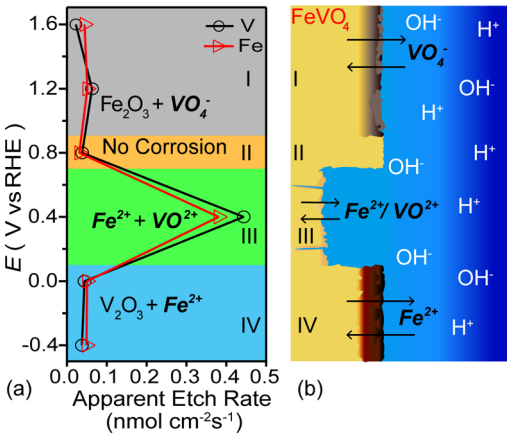

Figure 4. (a) Etching rate of Fe and V over 15 min aqueous electrochemical operations at pH 2.9 as a function of applied potential. The calculated stable species in the four pertinent voltage ranges, I–IV, are shown in background color where corroding species are in bold italics. (b) Schematic of the morphology of $FeVO_4$ in the presence of water under a steady state flow of the majority ions through the solid/liquid interface in regions I–IV corresponding to the voltage ranges marked in (a).

approximately half of the $FeVO_4$ film corroded away during the 15 min experiment, which is also supported by the XRD characterization of the sample (see Figure S2) which shows the same $FeVO_4$ pattern but with approximately half the intensity in the postelectrochemistry measurement compared to that in the as-prepared measurement. The XPS signal from this sample (Figure S3) shows a peak corresponding to Sn from the FTO conducting layer, indicating that some regions of the thin film dissolved completely.

No change in $FeVO_4$ was observed in XRD characterization of the samples held at other potentials (Figure S2). However, the postelectrochemistry measurements included a signal from the electrolyte salt, indicating that, upon drying of the samples, some electrolyte salts precipitated on each sample's surface. As a result, Na, S, and P were detected in the postelectrochemistry XRF signals (Figure 3). To understand the effect of the salt coating on the XRF measurement, we inspect the Si and Fe signals from the substrate and Sn signal from the FTO layer, whose slightly lowered intensity in the postelectrochemistry measurement demonstrates that the salt coating attenuates the XRF signal, resulting in a small apparent corrosion rate for both Fe and V even in the absence of corrosion. Consequently, Figure 4a provides an upper bound for the elemental etch rate of $FeVO_4$.

Only the 0.4 V sample exhibited substantial corrosion, which is consistent with the theoretical prediction that all decomposition products are solution-phase species at that condition. At all the remaining potentials, the elemental etch rates are nearly zero, in agreement with the theoretical results which predict that self-passivating coatings should be formed on the surface of $FeVO_4$. At 0.8 V, the XRD signal shows (see Figure S2) that the $FeVO_4$ crystal structure was unchanged, indicating that the $FeVO_4$ most likely did not transform to the predicted solid products ($Fe_2V_4O_{13}$ and Fe_2O_3). This could possibly be due to the relatively low driving force (ΔG_{pbx} = 0.336 eV/atom) for such a large solid–solid structural reorganization and no assistance from selective dissolution–precipitation processes as both Fe and V are predicted as stable against dissolution under these conditions.

The electrolyte salt coating on the electrochemically processed films resulted in relatively low Fe and V signals in the XPS spectra. The Fe 2p and V 2p XPS signals were compared with literature spectra for various species, indicating that the Fe^{3+} and V^{5+} species of the as-prepared film remain for films polarized at or above 0.8 V, which is commensurate with the prediction of phase stability and passivation by Fe_2O_3 in this voltage range. The films operated at −0.4 and 0 V contain lower-valent V, which is commensurate with the prediction of passivation by V_2O_3 under these conditions. Overall, these experiments demonstrate excellent agreement with the theoretical predictions and reveal that $FeVO_4$ does self-passivate at both low and high potential where a stable binary oxide is predicted to result from $FeVO_4$ decomposition.

Interestingly, at the potentials of −0.4 and 0 V, the XPS measurements show the presence of both Fe^{2+} and Fe^{3+} species (see Figure S3) in the film. The existence of Fe^{3+} species can be attributed to the pristine $FeVO_4$ bulk. However, the presence of Fe^{2+} species cannot be attributed to the formation of the V_2O_3 passivating layers or to the $FeVO_4$ bulk. In this context, we explain the presence of the Fe^{2+} species and the formation of the stable passivation layers using the concept of interfacial dissolution–precipitation processes and the Point Defect Model (PDM).[16,59,60] The PDM postulates the existence of highly defective interfacial passivation layers (cation vacancies, cation interstitials, and oxygen vacancies) that grow directly between the bulk and an exterior layer that forms via the hydrolysis of ions transmitted through the interfacial layer and the subsequent precipitation of a hydroxide, oxyhydroxide, or oxide depending upon the conditions. Under steady-state conditions, the thickness of the passivation layer is controlled by the standard rate constants for the generation of the defects in the interfacial layer and dissolution of ions through the interfacial and outer layers. The presence of Fe^{2+} in the $FeVO_4$ samples operated at −0.4 and 0 V supports the interchange between the liquid and solid phase, as the stable aqueous species is Fe^{2+}. The highly defective interfacial and outer layers could contain both Fe^{2+} and Fe^{3+} species in interstitial sites or in a locally disordered Fe–V–O phase; see voltage range IV of Figure 4b.

According to the PDM, while the formation of the passivating layers is a highly reactive thermodynamical process, the kinetic stability of the films is obtained through a steady state of defect generation and dissolution at the solid/passivation-layer/liquid interface. PDM predicts that the passivating films on $FeVO_4$ operated at 1.2 and 1.6 V are defective and disordered as well (see region I, Figure 4b); however, since the cations are in the same oxidations states both in the bulk material and the passivating films, XPS measurements are unable to corroborate the PDM predictions for this potential range. In total, all experimental results are commensurate with the model predictions.

SUMMARY AND CONCLUSIONS

In summary, we present a first-principles-based formalism to assess the propensity of thermodynamically stable as well as metastable materials toward electrochemical stabilization, passivation, or corrosion in aqueous media. This formalism allows us to evaluate the relative Gibbs free energy, ΔG_{pbx}, of arbitrary materials with respect to Pourbaix stable species at any

DOI: 10.1021/acs.chemmater.7b03980
Chem. Mater. 2017, 29, 10159–10167

pH, voltage, temperature, and concentration of ions. Comparing with experimental reports of 20 materials (including GaP, $Zn(FeO_2)_2$, Si, WSe_2, GaAs, Fe_2O_3, WO_3, and TiO_2) and our experimental investigations of the metastable triclinic-$FeVO_4$, we show that materials predicted to have ΔG_{pbx} up to 0.5 eV/atom may remain stable in aqueous media, depending on the nature of their predicted decomposition products. High driving force for decomposition (>0.5 eV/atom) and/or decomposition to only aqueous species is likely to cause corrosion. On the other hand, materials that exhibit decomposition to both aqueous and solid phases can exhibit self-passivation, by forming more stable solid phases at the interface. In this context, we find excellent agreement between experimentally measured and theoretically predicted compositions of passivation layers for materials which form passivation layers in water. Hence, the theoretical formalism presented here for estimating the electrochemical behavior of stable as well as metastable materials can be used to identify conditions under which arbitrary materials should form passivation layers and the composition of these passivation layers. This a priori knowledge of the passivation film composition can aid in parametrizing the Point Defect Model within the corrosion community. For instance, once the passivation composition is known from our first-principles calculations, the defect diffusion rates can be computed from atomistic simulations, such as DFT and molecular dynamics simulations. These parametrized PDMs can be further used to predict the passivation layer thickness and the electronic properties of the passivation layers.

Our work represents a clear advancement toward general corrosion management as well as for optimizing operating conditions of aqueous-media-based applications like photoelectrocatalysis. An open-source web application based on the formalism is available at https://materialsproject.org which can be used to determine the electrochemical behavior of more than 69 000 materials available through the Materials Project database. Moreover, we make the implementation of this formalism available via the Materials Project github repository at https://github.com/materialsproject/pymatgen, allowing the programmatic determination of electrochemical stability of arbitrary materials not included in the Materials Project database.

■ ASSOCIATED CONTENT

Supporting Information

The Supporting Information is available free of charge on the ACS Publications website at DOI: 10.1021/acs.chemmater.7b03980.

pH-dependent ΔG_{pbx} and decomposition products of all the photoanode materials at 1.5 V, physical vapor deposition-based synthesis procedure of $FeVO_4$, pre- and postelectrochemisty phase identification by XRD, composition measurements by XRF, and near-surface chemistry measurement by XPS (PDF)

■ AUTHOR INFORMATION

Corresponding Authors

*E-mail: arunimasingh@lbl.gov.
*E-mail: kapersson@lbl.gov.

ORCID

Arunima K. Singh: 0000-0002-7212-6310
Santosh K. Suram: 0000-0001-8170-2685
John M. Gregoire: 0000-0002-2863-5265

Notes

The authors declare no competing financial interest.

■ ACKNOWLEDGMENTS

This work was primarily funded by the Joint Center for Artificial Photosynthesis, a DOE Energy Innovation Hub, supported through the Office of Science of the U.S. Department of Energy under Award Number DE-SC0004993. Computational work was additionally supported by the Materials Project (Grant No. EDCBEE) Predictive Modeling Center through the U.S. Department of Energy (DOE), Office of Basic Energy Sciences, Materials Sciences and Engineering Division, under Contract DE-AC02-05CH11231. Computational resources were provided by the National Energy Research Scientific Computing Center, a DOE Office of Science User Facility supported by the Office of Science of the U.S. Department of Energy under Contract No. DE-AC02-05CH11231. The authors thank Matthias Richter for assistance with collection of XPS data.

■ REFERENCES

(1) Koch, G. H.; Brongers, M. P.; Thompson, N. G.; Virmani, Y. P.; Payer, J. H. *Corrosion cost and preventive strategies in the United States*; https://www.nace.org/Publications/Cost-of-Corrosion-Study/, 2002.

(2) Pourbaix, M. Atlas of electrochemical equilibria in aqueous solutions. https://www.amazon.com/Atlas-Electrochemical-Equilibria-Aqueous-Solutions/dp/0915567989, 1974.

(3) Takeno, N. Atlas of Eh-pH diagrams. *Geological Survey of Japan Open File Report* **2005**, *419*, 102.

(4) Brookins, D. G. *Eh-pH diagrams for geochemistry*; Springer Science & Business Media: New York, 2012.

(5) Persson, K. A.; Waldwick, B.; Lazic, P.; Ceder, G. Prediction of solid-aqueous equilibria: Scheme to combine first-principles calculations of solids with experimental aqueous states. *Phys. Rev. B: Condens. Matter Mater. Phys.* **2012**, *85*, 235438.

(6) Yan, Q.; Li, G.; Newhouse, P. F.; Yu, J.; Persson, K. A.; Gregoire, J. M.; Neaton, J. B. $Mn_2V_2O_7$: An earth abundant light absorber for solar water splitting. *Adv. Energy Mater.* **2015**, *5*, http://onlinelibrary.wiley.com/doi/10.1002/aenm.201401840/full.

(7) Zhou, L.; Yan, Q.; Yu, J.; Jones, R. J.; Becerra-Stasiewicz, N.; Suram, S. K.; Shinde, A.; Guevarra, D.; Neaton, J. B.; Persson, K. A.; Gregoire, J. M. Stability and self-passivation of copper vanadate photoanodes under chemical, electrochemical, and photoelectrochemical operation. *Phys. Chem. Chem. Phys.* **2016**, *18*, 9349−9352.

(8) Wills, L. A.; Qu, X.; Chang, I.-Y.; Mustard, T. J.; Keszler, D. A.; Persson, K. A.; Cheong, P. H.-Y. Group additivity-Pourbaix diagrams advocate thermodynamically stable nanoscale clusters in aqueous environments. *Nat. Commun.* **2017**, *8*, 15852.

(9) Koyama, M.; Zhang, Z.; Wang, M.; Ponge, D.; Raabe, D.; Tsuzaki, K.; Noguchi, H.; Tasan, C. C. Bone-like crack resistance in hierarchical metastable nanolaminate steels. *Science* **2017**, *355*, 1055−1057.

(10) Kazemi, F.; Saberi, A.; Malek-Ahmadi, S.; Sohrabi, S.; Rezaie, H.; Tahriri, M. Novel method for synthesis of metastable tetragonal zirconia nanopowders at low temperatures. *Ceram.-Silik.* **2011**, *55*, 26−30.

(11) Singh, A. K.; Mathew, K.; Zhuang, H. L.; Hennig, R. G. Computational screening of 2D materials for photocatalysis. *J. Phys. Chem. Lett.* **2015**, *6*, 1087−1098.

(12) Luo, G.; Yang, S.; Jenness, G. R.; Song, Z.; Kuech, T. F.; Morgan, D. Understanding and reducing deleterious defects in metastable alloy GaAsBi. *NPG Asia Mater.* **2017**, *9*, e345.

(13) Belsky, A.; Hellenbrandt, M.; Karen, V. L.; Luksch, P. New developments in the Inorganic Crystal Structure Database (ICSD): accessibility in support of materials research and design. *Acta Crystallogr., Sect. B: Struct. Sci.* **2002**, *58*, 364−369.

DOI: 10.1021/acs.chemmater.7b03980
Chem. Mater. 2017, 29, 10159−10167

(14) Sun, W.; Dacek, S. T.; Ong, S. P.; Hautier, G.; Jain, A.; Richards, W. D.; Gamst, A. C.; Persson, K. A.; Ceder, G. The thermodynamic scale of inorganic crystalline metastability. *Sci. Adv.* **2016**, *2*, e1600225.
(15) Wagman, D. D.; Evans, W. H.; Parker, V. B.; Schumm, R. H.; Halow, I. NBS tables of chemical thermodynamic properties. Selected values for inorganic and C1 and C2 organic substances in SI units. https://srd.nist.gov/JPCRD/jpcrdS2Vol11.pdf, 1982.
(16) Macdonald, D. On the existence of our metals based civilization. I. Phase-space analysis. 2006. *J. Electrochem. Soc.* **2006**, *153* (7), B213−B224.
(17) Jain, A.; Ong, S. P.; Hautier, G.; Chen, W.; Richards, W. D.; Dacek, S.; Cholia, S.; Gunter, D.; Skinner, D.; Ceder, G.; Persson, K. A. The Materials Project: A materials genome approach to accelerating materials innovation. *APL Mater.* **2013**, *1*, 011002.
(18) Saal, J. E.; Kirklin, S.; Aykol, M.; Meredig, B.; Wolverton, C. Materials design and discovery with high-throughput density functional theory: the open quantum materials database (OQMD). *JOM* **2013**, *65*, 1501−1509.
(19) Curtarolo, S.; Setyawan, W.; Wang, S.; Xue, J.; Yang, K.; Taylor, R. H.; Nelson, L. J.; Hart, G. L.; Sanvito, S.; Buongiorno-Nardelli, M.; Mingo, N.; Levy, O. AFLOWLIB.ORG: A distributed materials properties repository from high-throughputab initio calculations. *Comput. Mater. Sci.* **2012**, *58*, 227−235.
(20) Bale, C.; Bélisle, E.; Chartrand, P.; Decterov, S.; Eriksson, G.; Gheribi, A.; Hack, K.; Jung, I.-H.; Kang, Y.-B.; Melançon, J.; Pelton, A.; Petersen, S.; Robelin, C.; Sangster, J.; Spencer, P.; VanEnde, M.-A. FactSage thermochemical software and databases, 2010−2016. *CALPHAD: Comput. Coupling Phase Diagrams Thermochem.* **2016**, *54*, 35−53.
(21) Johnson, J. W.; Oelkers, E. H.; Helgeson, H. C. SUPCRT92: A software package for calculating the standard molal thermodynamic properties of minerals, gases, aqueous species, and reactions from 1 to 5000 bar and 0 to 1000 C. *Comput. Geosci.* **1992**, *18*, 899−947.
(22) Ong, S. P.; Cholia, S.; Jain, A.; Brafman, M.; Gunter, D.; Ceder, G.; Persson, K. A. The Materials Application Programming Interface (API): A simple, flexible and efficient API for materials data based on REpresentational State Transfer (REST) principles. *Comput. Mater. Sci.* **2015**, *97*, 209−215.
(23) Ong, S. P.; Richards, W. D.; Jain, A.; Hautier, G.; Kocher, M.; Cholia, S.; Gunter, D.; Chevrier, V. L.; Persson, K. A.; Ceder, G. Python Materials Genomics (pymatgen): A robust, open-source python library for materials analysis. *Comput. Mater. Sci.* **2013**, *68*, 314−319.
(24) Fujishima, A.; Honda, K. Electrochemical photolysis of water at a semiconductor electrode. *Nature* **1972**, *238*, 37−38.
(25) Liu, R.; Zheng, Z.; Spurgeon, J.; Yang, X. Enhanced photoelectrochemical water-splitting performance of semiconductors by surface passivation layers. *Energy Environ. Sci.* **2014**, *7*, 2504−2517.
(26) Yourey, J. E.; Pyper, K. J.; Kurtz, J. B.; Bartlett, B. M. Chemical stability of $CuWO_4$ for photoelectrochemical water oxidation. *J. Phys. Chem. C* **2013**, *117*, 8708−8718.
(27) Valenzuela, M.; Bosch, P.; Jiménez-Becerrill, J.; Quiroz, O.; Páez, A. Preparation, characterization and photocatalytic activity of ZnO, Fe_2O_3 and $ZnFe_2O_4$. *J. Photochem. Photobiol., A* **2002**, *148*, 177−182.
(28) De Haart, L.; Blasse, G. Photoelectrochemical properties of ferrites with the spinel structure. *J. Electrochem. Soc.* **1985**, *132*, 2933−2938.
(29) Beverskog, B.; Puigdomenech, I. Revised Pourbaix diagrams for iron at 25−300 °C. *Corros. Sci.* **1996**, *38*, 2121−2135.
(30) Ni, M.; Leung, M. K.; Leung, D. Y.; Sumathy, K. A review and recent developments in photocatalytic water-splitting using TiO_2 for hydrogen production. *Renewable Sustainable Energy Rev.* **2007**, *11*, 401−425.
(31) Hu, S.; Shaner, M. R.; Beardslee, J. A.; Lichterman, M.; Brunschwig, B. S.; Lewis, N. S. Amorphous TiO_2 coatings stabilize Si, GaAs, and GaP photoanodes for efficient water oxidation. *Science* **2014**, *344*, 1005−1009.
(32) Tang, D.; Mabayoje, O.; Lai, Y.; Liu, Y.; Mullins, C. B. Enhanced Photoelectrochemical Performance of Porous Bi_2MoO_6 Photoanode by an Electrochemical Treatment. *J. Electrochem. Soc.* **2017**, *164*, H299−H306.
(33) Zhang, L.; Baumanis, C.; Robben, L.; Kandiel, T.; Bahnemann, D. Bi_2WO_6 Inverse Opals: Facile Fabrication and Efficient Visible-Light-Driven Photocatalytic and Photoelectrochemical Water-Splitting Activity. *Small* **2011**, *7*, 2714−2720.
(34) Chen, X.; Yu, T.; Gao, F.; Zhang, H.; Liu, L.; Wang, Y.; Li, Z.; Zou, Z.; Liu, J.-M. Application of weak ferromagnetic $BiFeO_3$ films as the photoelectrode material under visible-light irradiation. *Appl. Phys. Lett.* **2007**, *91*, 022114.
(35) Moniz, S. J.; Quesada-Cabrera, R.; Blackman, C. S.; Tang, J.; Southern, P.; Weaver, P. M.; Carmalt, C. J. A simple, low-cost CVD route to thin films of $BiFeO_3$ for efficient water photo-oxidation. *J. Mater. Chem. A* **2014**, *2*, 2922−2927.
(36) Tolod, K. R.; Hernández, S.; Russo, N. Recent advances in the $BiVO_4$ photocatalyst for sun-driven water oxidation: Top-performing photoanodes and scale-up challenges. *Catalysts* **2017**, *7*, 13.
(37) Sayama, K.; Nomura, A.; Zou, Z.; Abe, R.; Abe, Y.; Arakawa, H. Photoelectrochemical decomposition of water on nanocrystalline $BiVO_4$ film electrodes under visible light. *Chem. Commun.* **2003**, 2908−2909.
(38) Toma, F. M.; Cooper, J. K.; Kunzelmann, V.; McDowell, M. T.; Yu, J.; Larson, D. M.; Borys, N. J.; Abelyan, C.; Beeman, J. W.; Yu, K. M. Mechanistic insights into chemical and photochemical transformations of bismuth vanadate photoanodes. *Nat. Commun.* **2016**, *7*, 12012.
(39) Courtin, E.; Baldinozzi, G.; Sougrati, M. T.; Stievano, L.; Sanchez, C.; Laberty-Robert, C. New Fe_2TiO_5-based nanoheterostructured mesoporous photoanodes with improved visible light photoresponses. *J. Mater. Chem. A* **2014**, *2*, 6567−6577.
(40) Doumerc, J.-P.; Hejtmanek, J.; Chaminade, J.-P.; Pouchard, M.; Krussanova, M. A photoelectrochemical study of $CuWO_4$ single crystals. *Phys. Status Solidi A* **1984**, *82*, 285−294.
(41) Nandjou, F.; Haussener, S. Degradation in photoelectrochemical devices: review with an illustrative case study. *J. Phys. D: Appl. Phys.* **2017**, *50*, 124002.
(42) Tang, D.; Rettie, A. J.; Mabayoje, O.; Wygant, B. R.; Lai, Y.; Liu, Y.; Mullins, C. B. Facile growth of porous $Fe_2V_4O_{13}$ films for photoelectrochemical water oxidation. *J. Mater. Chem. A* **2016**, *4*, 3034−3042.
(43) Seabold, J. A.; Neale, N. R. All first row transition metal oxide photoanode for water splitting based on $Cu_3V_2O_8$. *Chem. Mater.* **2015**, *27*, 1005−1013.
(44) Kalal, S.; Pandey, A.; Ameta, R.; Punjabi, P. B. Heterogeneous photo-Fenton-like catalysts $Cu_2V_2O_7$ and $Cr_2V_4O_{13}$ for an efficient removal of azo dye in water. *Cogent Chem.* **2016**, *2*, 1143344.
(45) Mandal, H.; Shyamal, S.; Hajra, P.; Bera, A.; Sariket, D.; Kundu, S.; Bhattacharya, C. Development of ternary iron vanadium oxide semiconductors for applications in photoelectrochemical water oxidation. *RSC Adv.* **2016**, *6*, 4992−4999.
(46) Morton, C. D.; Slipper, I. J.; Thomas, M. J.; Alexander, B. D. Synthesis and characterisation of Fe-V-O thin film photoanodes. *J. Photochem. Photobiol., A* **2010**, *216*, 209−214.
(47) Guo, W.; Chemelewski, W. D.; Mabayoje, O.; Xiao, P.; Zhang, Y.; Mullins, C. B. Synthesis and characterization of CuV_2O_6 and $Cu_2V_2O_7$: Two photoanode candidates for photoelectrochemical water oxidation. *J. Phys. Chem. C* **2015**, *119*, 27220−27227.
(48) Tenne, R.; Wold, A. Passivation of recombination centers in *n*-WSe_2 yields high efficiency (> 14%) photoelectrochemical cell. *Appl. Phys. Lett.* **1985**, *47*, 707−709.
(49) Meissner, D.; Benndorf, C.; Memming, R. Photocorrosion of cadmium sulfide: Analysis by photoelectron spectroscopy. *Appl. Surf. Sci.* **1987**, *27*, 423−436.
(50) Yamada, S.; Nosaka, A. Y.; Nosaka, Y. Fabrication of CdS photoelectrodes coated with titania nanosheets for water splitting with visible light. *J. Electroanal. Chem.* **2005**, *585*, 105−112.

DOI: 10.1021/acs.chemmater.7b03980
Chem. Mater. 2017, 29, 10159−10167

(51) Schmuki, P.; Sproule, G.; Bardwell, J.; Lu, Z.; Graham, M. Thin anodic oxides formed on GaAs in aqueous solutions. *J. Appl. Phys.* **1996**, *79*, 7303−7311.
(52) Wang, H.-H.; Wu, J.-Y.; Wang, Y.-H.; Houng, M.-P. Effects of pH Values on the Kinetics of Liquid-Phase Chemical-Enhanced Oxidation of GaAs. *J. Electrochem. Soc.* **1999**, *146*, 2328−2332.
(53) Lee, M. H.; Takei, K.; Zhang, J.; Kapadia, R.; Zheng, M.; Chen, Y.-Z.; Nah, J.; Matthews, T. S.; Chueh, Y.-L.; Ager, J. W.; Javey, A. *p*-Type InP Nanopillar Photocathodes for Efficient Solar-Driven Hydrogen Production. *Angew. Chem., Int. Ed.* **2012**, *51*, 10760−10764.
(54) Radhakrishnan, B.; Ong, S. P. Aqueous stability of alkali superionic conductors from first-principles calculations. *Front. Energy Res.* **2016**, *4*, 16.
(55) Lian, X.; Xiao, P.; Liu, R.; Henkelman, G. Calculations of oxygen adsorption-induced surface reconstruction and oxide formation on Cu (100). *Chem. Mater.* **2017**, *29*, 1472−1484.
(56) Duan, Z.; Henkelman, G. CO oxidation on the Pd (111) surface. *ACS Catal.* **2014**, *4*, 3435−3443.
(57) Barmak, K.; Liu, J.; Harlan, L.; Xiao, P.; Duncan, J.; Henkelman, G. Transformation of topologically close-packed β-W to body-centered cubic α-W: Comparison of experiments and computations. *J. Chem. Phys.* **2017**, *147*, 152709.
(58) Guo, Y.; Sun, D.; Ouyang, B.; Raja, A.; Song, J.; Heinz, T. F.; Brus, L. E. Probing the dynamics of the metallic-to-semiconducting structural phase transformation in MoS_2 crystals. *Nano Lett.* **2015**, *15*, 5081−5088.
(59) Macdonald, D. D. Theory of passive film stability. *ECS Trans.* **2006**, *2*, 73−81.
(60) Obot, I.; Macdonald, D.; Gasem, Z. Density functional theory (DFT) as a powerful tool for designing new organic corrosion inhibitors. Part 1: an overview. *Corros. Sci.* **2015**, *99*, 1−30.

DOI: 10.1021/acs.chemmater.7b03980
Chem. Mater. 2017, 29, 10159−10167